# **Inorganic Chemistry**

pubs.acs.org/IC Article

# Electron Density Analysis of Metal—Metal Bonding in a Ni<sub>4</sub> Cluster Featuring Ferromagnetic Exchange

Sofie Stampe Leiszner, Khetpakorn Chakarawet, Jeffrey R. Long, Eiji Nishibori, Kunihisa Sugimoto, James A. Platts, and Jacob Overgaard\*



Cite This: Inorg. Chem. 2023, 62, 192-200



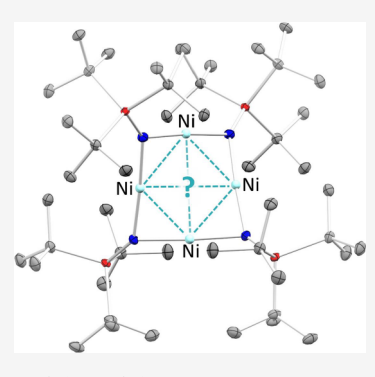
**ACCESS** I

Metrics & More

Article Recommendations

s) Supporting Information

**ABSTRACT:** We present a combined experimental and theoretical study of the nature of the proposed metal—metal bonding in the tetranuclear cluster  $Ni_4(NP^tBu_3)_4$ , which features four nickel(I) centers engaged in strong ferromagnetic coupling. High-resolution single-crystal synchrotron X-ray diffraction data collected at 25 K provide an accurate geometrical structure and a multipole model electron density description. Topological analysis of the electron density in the  $Ni_4N_4$  core using the quantum theory of atoms in molecules clearly identifies the bonding as an eight-membered ring of type  $[Ni-N-]_4$  without direct Ni-Ni bonding, and this result is generally corroborated by an analysis of the energy density distribution. In contrast, the calculated bond delocalization index of  $\sim$ 0.6 between neighboring Ni atoms is larger than what has been found for other bridged metal—metal bonds and implies direct Ni-Ni bonding. Similar support for the presence of direct Ni-Ni bonding is found in the interacting quantum atom approach, an energy decomposition scheme, which suggests the presence of stabilizing



Ni—Ni bonding interactions with an exchange-correlation energy contribution approximately 50% of that of the Ni—N interactions. Altogether, while the direct interactions between neighboring Ni centers are too weak and sterically constrained to bear the signature of a topological bond critical point, other continuous measures clearly indicate significant Ni—Ni bonding. These metal—metal bonding interactions likely mediate direct ferromagnetic exchange, giving rise to the high-spin ground state of the molecule.

#### INTRODUCTION

The topic of chemical bonding is of integral importance for understanding the magnetic properties of molecular and extended solids. Metal-metal bonding, in particular, underpins the properties of lanthanide-based permanent magnets and has recently been exploited in molecular lanthanide compounds to achieve record coercivities.<sup>2</sup> In certain multinuclear transition metal complexes, direct metal-metal orbital overlap has also been shown to give rise to strong ferromagnetic coupling and thermally isolated large spin ground states, as well as single-molecule magnetism due to the suppression of quantum tunneling of magnetization.<sup>3-6</sup> Among these compounds, the tetranuclear species  $M_4(NP^{t}Bu_3)_4^{+/0}$  (M = Co, Ni, Cu;  ${}^{t}Bu = tert$ -butyl)<sup>7</sup> represent an interesting case study. 8,9 The coordination geometry of the metal ions in these complexes is rather unusual: each metal is coordinated to two nitrogen atoms in a nearly linear fashion, creating an eight-membered (MN-)4 ring, with all four metal atoms residing in a plane dictated by a crystallographic twofold rotation axis and nitrogen atoms alternating above and below this plane. In the case of the neutral compound Ni<sub>4</sub>(NP<sup>t</sup>Bu<sub>3</sub>)<sub>4</sub>, computational analysis indicated a partial, direct metal-metal bonding interaction that leads to an isolated ground-state molecular spin of S = 2.8 Density functional theory (DFT) calculations predicted four unpaired electrons residing in the metal-ligand antibonding orbitals with partial metal-metal antibonding character. If these four orbitals  $(4b_1^*, 2a_2^*, and 6e^*)$  are considered metal—metal antibonding and the three remaining metal—ligand antibonding orbitals  $(5e^* \text{ and } 3a_1^*)$  are considered metal—metal bonding, a total metal—metal bond order of two is obtained for 1.

In contrast to a molecular orbital picture of bonding, wherein the contribution of each molecular orbital to the chemical bonding is assessed individually, the quantum theory of atoms in molecules  $(QTAIM)^{10}$  operates exclusively on the total electron density distribution. Partitioning the electron density of the molecule into individual Bader atomic basins allows for an unbiased analysis of interatomic interactions. This topological analysis yields so-called critical points that are classified by two numbers: the number of nonzero Hessian eigenvalues (the rank, m) and the algebraic sum of the signs of the Hessian eigenvalues (the signature, n). For example, a (3,-1) bond critical point is a minimum in electron density along the bonding direction but a maximum in the two remaining directions, corresponding to one positive and two negative

Received: September 6, 2022 Published: December 22, 2022





eigenvalues of the Hessian matrix, yielding a signature of -1. The QTAIM is rooted in quantum mechanics and has been used to study metal—metal bonding in a variety of molecular and extended solids.  $^{11-28}$  A landmark study summarizing the strengths of this approach was published by Macchi et al., wherein the authors compared the molecular graphs for various cobalt cluster complexes with and without bridging ligands. It was shown that the direct metal—metal bond path disappeared and nearly straight metal—ligand bond paths emerged when a bridging ligand was introduced.

Herein, we present the results of a detailed study of chemical bonding in the central  $Ni_4N_4$  moiety of  $Ni_4(NP^tBu_3)_4$  (1). We begin by deriving a multipole model for the experimental electron density of 1 based on high-resolution single-crystal synchrotron X-ray diffraction data obtained at low temperatures (Figure 1). We experimentally evaluate the chemical

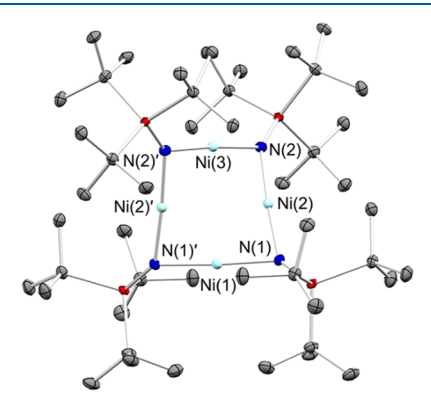


**Figure 1.** Single-crystal X-ray diffraction structure of **1** shown with 50% probability ellipsoids. Light blue, red, dark blue, and gray ellipsoids represent Ni, P, N, and C atoms, respectively; hydrogen atoms and the disordered hexane molecules have been omitted for clarity. The compound features a twofold axis running through Ni(1) and Ni(3). Average Ni···Ni distances for neighboring and diagonal Ni centers are 2.36079(4) and 3.33680(5) Å, respectively, and the average Ni–N distance is 1.8545(2) Å. Average N–Ni–N and Ni–N–Ni angles are 180.25(1)° and 79.063(5)°, respectively.

bonding based on the QTAIM via inclusion of a topological analysis of both the electron density and the total energy density. As previously established, **1** exhibits an S=2 molecular ground state, and complete active space self-consistent field (CASSCF) analysis indicated that the four Ni sites are ferromagnetically coupled, with a computed electron-transfer energy of 6.1 eV between the adjacent Ni ions being the dominant exchange pathway. A major goal of the current study was to investigate whether the experimental electron density is able to detect such highly delocalized bonding. We additionally present results from delocalization indices and interacting quantum atom energy-partitioning as derived from computations.

#### EXPERIMENTAL SECTION

Synthesis and Single-Crystal X-Ray Diffraction Analysis. The compound Ni<sub>4</sub>(NP<sup>t</sup>Bu<sub>3</sub>)<sub>4</sub> (1) was synthesized and crystallized using a previously published procedure. One molecule of hexane cocrystallizes with each tetranuclear cluster in the solid-state structure. Single-crystal X-ray diffraction data were collected at the BL02B1 beamline at SPring-8 in Japan. The crystal was cooled to 25 K, and six 180°  $\omega$  scans ( $\Delta\omega=0.1^\circ$ ) were carried out with  $\chi$  positioned at 0°, 20°, and 40°, using 2 $\theta$ -values of 0° and -10°. Data were collected with a Dectris PILATUS3 X 1 M CdTe detector ( $\lambda=0.248233$  Å). A local

program (Pilatus-fc) $^{29}$  was used to convert the obtained data to files readable by APEX3,  $^{30}$  Lorentz and polarization-corrected integrated intensities were obtained using Saint V8.38A  $^{31}$  up to a maximum resolution of  $\sin(\theta)/\lambda=1.11~{\rm \AA}^{-1}.$  Scale frame factors were refined using SADABS,  $^{32}$  while the program SORTAV  $^{33}$  was used to merge equivalent reflections. The structure was solved with ShelXT,  $^{34}$  while ShelXL  $^{35}$  was used for structure refinement. Hydrogen atoms were included in a riding model using the AFIX-137 command in ShelXL. The resulting geometry was used as a starting point for the multipole refinement in the program XD2016.  $^{36}$ 

**Experimental Multipole Modeling.** The multipole model formalism introduced by Hansen and Coppens<sup>37</sup> was used to describe the electron density. The multipole model partitions the electron density into three separate components: the spherical core density, the spherical valence density, and the aspherical valence density. Each component corresponds to a term in eq 1 below:

$$\rho_{\text{atom}}(\mathbf{r}) = P_{o}\rho_{c}(\mathbf{r}) + P_{v}\kappa^{3}\rho_{v}(\kappa\mathbf{r}) + \sum_{l=0}^{l_{\text{max}}} \kappa'^{3}R_{l}(\kappa'\mathbf{r}) \sum_{m=0}^{l} P_{lm\pm}d_{lm\pm}(\theta, \varphi)$$
(1)

where  $P_{\rm c}$ ,  $P_{\rm v}$ , and  $P_{lm\pm}$  are the multipole population parameters for the core, spherical valence, and aspherical valence density, respectively, and  $\kappa$  and  $\kappa'$  are the expansion/contraction parameters for the spherical and aspherical parts of the valence electron density, respectively. The radial functions,  $R_l(\kappa'r)$ , are nodeless, single-zeta Slater functions with optimized coefficients and exponents. The functions denoted  $d_{lm\pm}$  are angular orbital-like functions. To enhance aspherical features, we used the Laplacian of the electron density. The negative of the Laplacian will have maxima in regions of accumulated density and minima in the regions of charge depletion.  $^{39}$ 

In the development of a multipole model, it is important to consider the choice of the local coordinate system. First, any local noncrystallographic symmetry may significantly reduce the number of multipole parameters of a given atom, which improves convergence issues and limits possible correlations between parameters. The applied symmetries in the initial refinements are listed in Table S2. Second, the analysis of the d-orbital distribution on metal atoms is completely tied to the choice of x, y, z axes. The choice of the local coordinate system for the Ni atoms is displayed in Figure S1.

As seen from Figure 1, compound 1 features a twofold axis passing through Ni(1) and Ni(3), which constrains the positional and thermal parameters on these two atoms. Additional constraints were added for hydrogen atoms, for which specific C–H bond distances were set depending on the bonding environment. The values are based on tabulated neutron diffraction data. 40 In addition, isotropic atomic displacement parameters (ADPs) of the hydrogen atoms were also constrained such that they depend on the anisotropic ADPs of the atom to which they are bonded. Atoms in the compound with similar chemical environments were furthermore constrained by multipole population constraints in the initial refinements. Refinement details are provided in the Supporting Information.

Refinement of the multipole model revealed systematic errors in the diffraction data (Figure S3, gray data), which we ascribe to thermal diffuse scattering, which is inelastic scattering and variably affects the integrated intensities in the X-ray diffraction experiment. This type of scattering can be corrected according to a procedure published by Niepotter et al., 41 which substantially improves the model as seen from the fractal dimensionality plot in Figure S3. 42

**Theoretical Multipole Model.** Metal—metal bonding in 1 was previously analyzed using DFT. Here, to enable a comparison between the experimental model for 1 and the theoretical model in the same multipole framework, theoretical structure factors were obtained from a DFT calculation performed on 1. The theoretical structure factors,  $F_{\rm H}$ , were calculated as a Fourier transform of the electron density:

$$F_{\mathbf{H}} = Tr[\mathbf{D}^{0}\mathbf{I}^{\mathbf{H}}] \tag{2}$$

where  $D^0$  is a one-electron density matrix, and  $I^H$  is a matrix of the averaged Fourier integrals of the basis function products.<sup>43</sup> In the

current study, ORCA was used with the B3LYP functional and def2-SV(P) basis set and auxiliary basis sets generated by ORCA. 44,45 The calculation was based on the experimental atomic positions in 1 determined at 25 K, excluding the hexane molecule. The resulting quasi-restricted orbitals appear visually very similar to those previously reported (Figure S6).8 To calculate the theoretical structure factors, a fictitious crystal structure was created by placing one molecule of 1 inside a  $20 \times 20 \times 20 \text{ Å}^3$  cubic unit cell without symmetry, and subsequently, the theoretical structure factors were calculated, which were then used to obtain a theoretical multipole model for comparison with the experiment. The basis functions used in the multipole model are different from those used in the DFT calculation. Thus, some residual density is expected after the refinement. To improve the theoretical model, all atoms were split into two parts: one containing the core electrons and another containing the valence electrons. This approach enables the electron density belonging to the core of the atoms to be described in a more flexible manner with their own  $\kappa$ -parameters. The fractal dimensionality plot for the theoretical model of 1 is shown in Figure S4. Based on the narrow parabola shape seen in the plot, there are no indications of systematic errors in the model.

**Total Energy Density.** It has been shown that the total energy density, H(r), is more sensitive for analyzing bonding effects than the electron density itself or the Laplacian of the electron density. <sup>46,47</sup> The total energy density is the sum of the kinetic energy density, G(r), and the potential energy density, V(r):

$$H(r) = G(r) + V(r) \tag{3}$$

Analysis of the total energy density for the theoretical model of 1 was performed using the AIMAll software.  $^{48}$ 

**Interacting Quantum Atom Analysis.** Within the QTAIM analysis, the molecular energy can be partitioned into the following one- and two-basin contributions:

$$E = \sum_{A} \int_{\Omega_{A}} d\mathbf{r}_{1} \left[ \hat{T} - \sum_{B} \frac{Z_{B}}{r_{1B}} \right] \rho_{1}(\mathbf{r}_{1}; \mathbf{r}_{1}')$$

$$+ \frac{1}{2} \sum_{A,B} \int_{\Omega_{A}} d\mathbf{r}_{1} \int_{\Omega_{B}} d\mathbf{r}_{2} \frac{\rho_{2}(\mathbf{r}_{1}; \mathbf{r}_{2})}{r_{12}} + \sum_{A>B} \frac{Z_{A}Z_{B}}{R_{AB}}$$
(4)

where  $\Omega_A$  is the atomic basin of atom A, and  $\rho_1(r_1; r_1')$  and  $\rho_2(r_1; r_2)$  are the first- and second-order reduced density matrices, respectively.  $\rho_2(r_1; r_2)$  can be decomposed into a Coulombic and an exchange correlation contribution:

$$\rho_2(\mathbf{r}_1; \, \mathbf{r}_2) = \rho(\mathbf{r}_1)\rho(\mathbf{r}_2) - \rho_2^{\text{xc}}(\mathbf{r}_1; \, \mathbf{r}_2) \tag{5}$$

By rearranging eq 4, it can be shown that the energy can be partitioned into the following two terms: the atomic self-energy defined by the intrabasin contributions and the sum of all interbasin energies.

$$E = \sum_{A} (T_{A} + V_{en}^{AA} + V_{ee}^{AA}) + \sum_{A>B} (V_{nn}^{AB} + V_{en}^{AB} + V_{en}^{BA} + V_{ee}^{AB})$$

$$= \sum_{A} E_{self}^{A} + \sum_{A>B} E_{int}^{AB}$$
(6)

The term  $V_{\rm ee}^{\rm AB}$  in eq 6 has two contributions, a purely Coulombic term,  $V_{\rm C}^{\rm AB}$ , and an exchange-correlation contribution,  $V_{\rm xc}^{\rm AB}$ . These are defined as follows:

$$V_{\rm C}^{\rm AB} = \int_{\Omega_{\rm A}} \mathrm{d}\mathbf{r}_1 \int_{\Omega_{\rm B}} \mathrm{d}\mathbf{r}_2 \frac{\rho(\mathbf{r}_1)\rho(\mathbf{r}_2)}{r_{12}} \tag{7}$$

$$V_{\text{xc}}^{\text{AB}} = -\int_{\Omega_{\text{A}}} d\mathbf{r}_1 \int_{\Omega_{\text{B}}} d\mathbf{r}_2 \frac{\rho^{\text{xc}}(\mathbf{r}_1; \mathbf{r}_2)}{\mathbf{r}_{12}}$$
(8)

In this way, the interaction energy between atoms A and B,  $E_{\rm int}^{\rm AB}$ , in eq 6 can be further composed into two terms:

$$E_{\rm int}^{\rm AB} = V_{\rm cl}^{\rm AB} + V_{\rm xc}^{\rm AB} \tag{9}$$

where the Coulombic term,  $V_{cl}^{AB}$ , is the classical interaction energy:

$$V_{\rm cl}^{\rm AB} = V_{\rm nn}^{\rm AB} + V_{\rm en}^{\rm AB} + V_{\rm en}^{\rm BA} + V_{\rm C}^{\rm AB} \tag{10}$$

and the exchange correlation term,  $V_{\rm xc}^{\rm AB}$ , contains the covalent interaction between atoms A and B.  $^{49}$ 

Determination of the interaction energy in eq 9 requires a wavefunction, which was obtained from a DFT calculation for 1. All atomic basins were initially found, and the three terms in eq 9 were then determined from the desired atom pairs. The calculations were carried out with the AIMAll software.<sup>48</sup>

**Bond Delocalization Index.** We also employed the delocalization index to investigate the bonding properties in 1. 50,51 At the Hartree–Fock level, the delocalization index can be interpreted as the number of electron pairs shared between two basins 17 and is calculated according to eq 11:

$$\delta(A, B) = 2 \int_{\Omega_{A}} d\mathbf{r}_{1} \int_{\Omega_{B}} d\mathbf{r}_{2} \rho_{2}^{xc}(\mathbf{r}_{1}; \mathbf{r}_{2})$$

$$\tag{11}$$

The two basins,  $\Omega_A$  and  $\Omega_B$ , do not need to have a common interatomic surface for the delocalization index to be determined, meaning that the delocalization index can be calculated for any pair of atoms, regardless of whether or not they are formally bonded. Delocalization indices are only available from theoretical densities and were calculated from the theoretical wave function of 1 using the program AIMAII, which first integrates the atomic basins and subsequently determines the delocalization index between each atom pair in the cluster. We note that while DIs and the underlying two-particle density are not fully defined in Kohn-Sham DFT, their use in this context is common and widely accepted.

#### RESULTS AND DISCUSSION

Low-Temperature Molecular Structure. The molecular structure of 1 determined at 25 K is shown in Figure 1 (see the caption for selected average angles and distances and Tables S2 and S3 for additional bond distances and angles). As previously reported, the compound crystallizes in the space group C2/c with a single hexane molecule in the unit cell. The asymmetric unit consists of half a molecule, with the other half generated by a twofold rotation through Ni(1) and Ni(3), such that the four metal atoms are exactly in the same plane. Each of the four [tBu3PN] ligands bridges two Ni ions through nitrogen, forming the vertices of a distorted molecular square cluster with nearly linear N-Ni-N edges (average N-Ni-N angle of 180.25°). Each N adopts a distorted trigonal planar geometry, with average P-N-Ni and Ni-N-Ni angles of 138.7° and 79.1°, respectively. The average distance between neighboring Ni atoms is 2.361 Å, in good agreement with the previously reported structure of 1.<sup>7,8</sup> This Ni···Ni separation is within the range of reported distances for Ni-Ni single bonds; 53 thus, the geometry does not exclude the possibility for direct metalmetal bonding between neighboring Ni centers. Of note, there are significant differences between the two Ni···Ni distances across the Ni<sub>4</sub>-square. The distance between Ni(1) and Ni(3) along the twofold rotation is 3.448 Å, whereas that between Ni(2) and Ni(2)' is only 3.225 Å. The Ni<sub>4</sub> square is thus slightly asymmetric; however, the Ni atoms experience similar local chemical environments.

Electron Density Analysis of Ni···Ni Interactions. The main purpose of this work was to study the nature of chemical bonding in the central  $Ni_4N_4$  moiety in 1. The static deformation density is a relevant tool for this purpose, given that it highlights the aspherical features of the electron density by showing accumulated density in the bonding and lone-pair regions. The static deformation density is the difference between the density from the experimental or theoretical

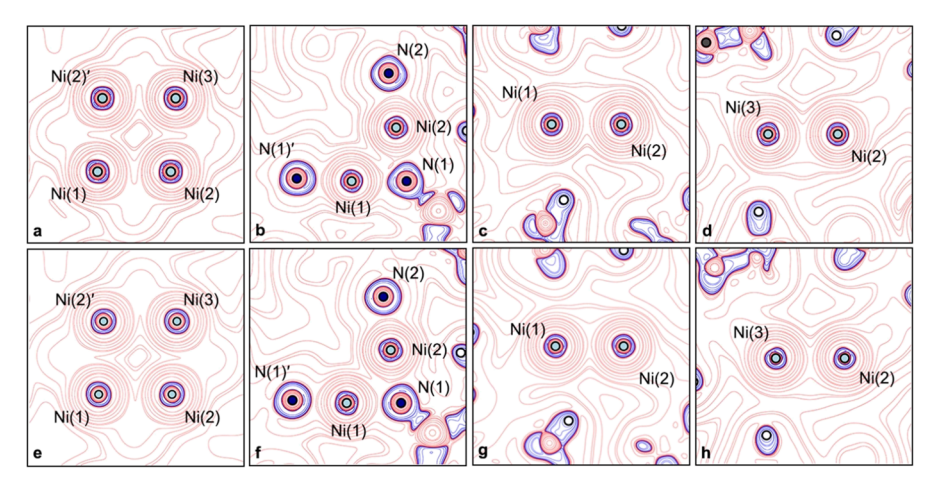


Figure 2. Two-dimensional plots of the negative Laplacian for the experimental (a-d) and theoretical (e-h) model of 1 in several different planes: (a,e) in the Ni<sub>4</sub>-plane; (b,f) in the Ni<sub>4</sub>-plane; (b,f) in the Ni<sub>4</sub>-plane; (c,g) in the plane perpendicular to the Ni<sub>4</sub>-plane through Ni(1) and Ni(2); and (d) and (h) in the plane perpendicular to the Ni<sub>4</sub>-plane through Ni(2) and Ni(3). The solid blue lines indicate positive contours in the negative Laplacian,  $\nabla^2 \rho(r) < 0$ , and the dashed red lines indicate negative contours in the negative Laplacian,  $\nabla^2 \rho(r) > 0$ . Contours are drawn at  $\pm 2 \times 10^n$ ,  $\pm 4 \times 10^n$ , and  $\pm 8 \times 10^n$  e Å<sup>-5</sup> ( $n = \pm 3, \pm 2, \pm 1, 0$ ).

multipole model and the density from the independent atom model<sup>54</sup> and is plotted in four different two-dimensional (2D) planes for the experimental and theoretical models of 1 in Figures S7 and S8. Figure S7b clearly shows the pronounced, direct Ni–N bonding as positive deformation density, indicating that more electron density is located here in the multipole model compared to the independent atom model.

In the original study of the magnetism of 1,8 it was suggested that the bonding between neighboring Ni atoms possesses some degree of  $\pi$ -character; thus, Figure S8a,b shows the experimental and theoretical deformation density in planes perpendicular to the Ni<sub>4</sub> plane. In Figure S8a, the plane bisects Ni(1) and Ni(2), whereas Ni(2) and Ni(3) are bisected in Figure S8b. In the theoretical model, there is positive deformation density in an extended region covering neighboring Ni atoms on one side of the Ni<sub>4</sub> plane, as shown in Figure S8a,b. This could in fact be interpreted as a signature of neighboring Ni atoms being involved in direct  $\pi$ -bonding; however, the positive deformation density is only present on one side of the Ni<sub>4</sub> plane, which is where the bridging nitrogen atom is located. Thus, this observed accumulation of electron density can be ascribed to the periphery of the Ni-N bonding, which is seen as large positive contours, as shown in Figure S7b. These plots demonstrate the potential limitations of relying solely on 2D slicing through the three-dimensional electron density. In general, the unusual coordination environment around the Ni centers in 1 makes definite conclusions regarding the chemical bonding difficult to draw using the deformation density.

To derive more accurate insights into the chemical bonding in 1, we examined the Laplacian of the electron density  $(\nabla^2 \rho(r))$ , which can be used to identify local charge depletions  $(\nabla^2 \rho(r) > 0)$  and charge concentrations  $(\nabla^2 \rho(r) < 0)$ . The calculated Laplacian is shown in Figure 2 in various planes for both the experimental and theoretical models of 1. The plots in Figure 2a,b,e,f show no sign of charge accumulation between the Ni atoms. In the Ni<sub>4</sub>-plane shown in Figure 2a,e, the valence shell charge concentrations on all Ni atoms (represented by blue contour lines) are seen perpendicular to the diagonal Ni···Ni direction. In Figure 2b,f, the two maxima of the Laplacian in the valence shell of N(1) point

toward the valence shell depletion regions on Ni(1) and Ni(2) in the typical key-lock fashion.<sup>55</sup>

Ultimately, neither the analysis of the static deformation density (Figures S7 and S8) nor the Laplacian (Figure 2) gives a clear indication of whether there is direct Ni–Ni bonding. The primary reason is that the spatial prevalence of the Ni–N bonding features into the adjacent Ni···Ni interatomic region and renders clear conclusions impossible. On the other hand, a topological analysis of the electron density supports the absence of direct Ni–Ni bonding. Figure 3 displays all the bond paths and associated critical points—the so-called molecular graph—for the Ni<sub>4</sub>N<sub>4</sub> unit. This representation shows highly directional Ni–N bonding in what becomes an eight-membered ring structure with a ring critical point at the center, and there are no signs of bonding interactions between Ni centers. The values of the electron density at the bond

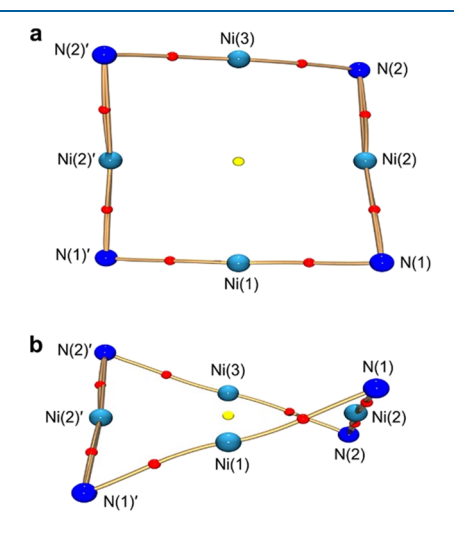


Figure 3. Overhead (a) and side (b) views of the molecular graph of the critical points in the electron density for the experimental model of 1. The red and yellow spheres are (3, -1) and (3, +1) critical points, respectively. Bond paths and straight lines between bonding atoms are marked with golden cylinders. Light blue and dark blue spheres represent Ni and N atoms, respectively. A similar molecular graph is obtained for the theoretical model of 1 (Figure S9).

critical points,  $\rho_{\rm b}$ , and the Laplacian,  $\nabla^2\rho_{\rm b}$ , are listed in Table S4.

Energy Density Analysis of Ni···Ni Interactions. While our analysis of the electron density revealed no indication of bonding between the Ni atoms, it must be acknowledged that the classification of metal-metal bonds is a complicated matter, for which a localized description such as the QTAIM analysis has proven insufficient on several occasions, <sup>17</sup> and the use of other descriptors has been encouraged. 46,56 An important factor causing ambiguity in the topology around these metal-metal bonding regions is the fact that the electron density landscape is often rather flat.<sup>17</sup> This point is perhaps best exemplified by the study of metal···metal interactions in metal carbonyl complexes, which bear some structural resemblance to 1, given their very acute bond angles and bridging ligands. Chemical knowledge (principally the 18electron rule and short metal...metal distances) unambiguously point to the presence of metal-metal bonding in compounds, such as Fe<sub>2</sub>(CO)<sub>9</sub> and the bridged and unbridged isomers of Co<sub>2</sub>(CO)<sub>8</sub>. 56-61 However, topological analysis of the electron density does not consistently reveal bond critical points between the metal atoms in such compounds. Furthermore, a study of Fe<sub>2</sub>(CO)<sub>9</sub> by Reinhold et al. found that the type of critical point between the two Fe atoms was highly dependent upon the basis set used in the calculation.<sup>57</sup> Similarly, a topological analysis of the electron density in the bridged Co<sub>2</sub>(CO)<sub>8</sub> complex failed to show a direct Co-Co bond critical point. In contrast, the total energy density produced a distinct minimum in  $H(\mathbf{r})$ , coinciding with the midpoint of the hypothetical Co-Co bond, suggesting that the energy density may afford a clearer view of the properties of these weak metal-metal bonds.<sup>56</sup> This point is also apparent from an electron density study of the dinuclear bridged complex  $Co_2(CO)_6(HC \equiv CC_6H_{10}OH)$ . While a bond critical point was not observed in the electron density, inspection of the total energy density did indicate a stabilizing interaction between the Co atoms in the Co<sub>2</sub>C triangle.<sup>26</sup>

Considering these studies, we also explored the energy density distribution in 1. In an extension of the previous work described above, where the energy density was qualitatively examined only along a select few lines, we present here also a full topological analysis of this property. The topology of  $K(\mathbf{r})$  $= -H(\mathbf{r})$  can be analyzed in the same way as the electron density, and an analogous "molecular graph" can be created (see Figure 4). In complete accordance with the electron density, the topology of the energy density recovers the ring structure with eight (3, -1) critical points forming the (Ni- $N-)_4$  chain and a central (3, +1) critical point. However, additional critical points appear in the analysis of  $K(\mathbf{r})$  in the Ni<sub>4</sub> square along with their symmetry-related critical points: two (3, -1) critical points linking Ni(2) and Ni(2)' across the diagonal of the  $Ni_4$  square and four (3, -3) critical points located in the Ni-N-Ni planes between neighboring Ni atoms. Recalling that  $H(\mathbf{r}) = -K(\mathbf{r})$ , the (3, -3) critical points correspond to local minima in  $H(\mathbf{r})$ , and each minimum may be interpreted as the signature of a stabilizing interaction (see Figure S10 for visualization of one such minimum in the plot of  $H(\mathbf{r})$  from Ni(1) to Ni(2)). Thus, in all, our exploration of chemical bonding between the Ni centers in 1 using topological analysis provides rather ambiguous results (Figure 5).

**Interacting Quantum Atoms.** We turned to the interacting quantum atoms (IQA) approach to examine the

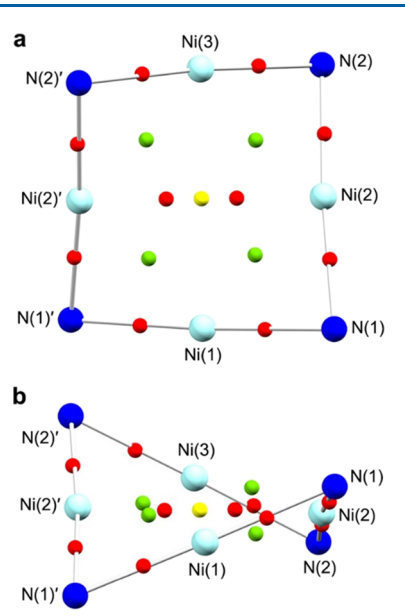


**Figure 4.** Overhead (a) and side (b) views of the molecular graph of the critical points in  $K(\mathbf{r})$  for the theoretical wavefunction of 1. Red, green, and yellow spheres are (3, -1), (3, -3), and (3, +1) critical points, respectively.

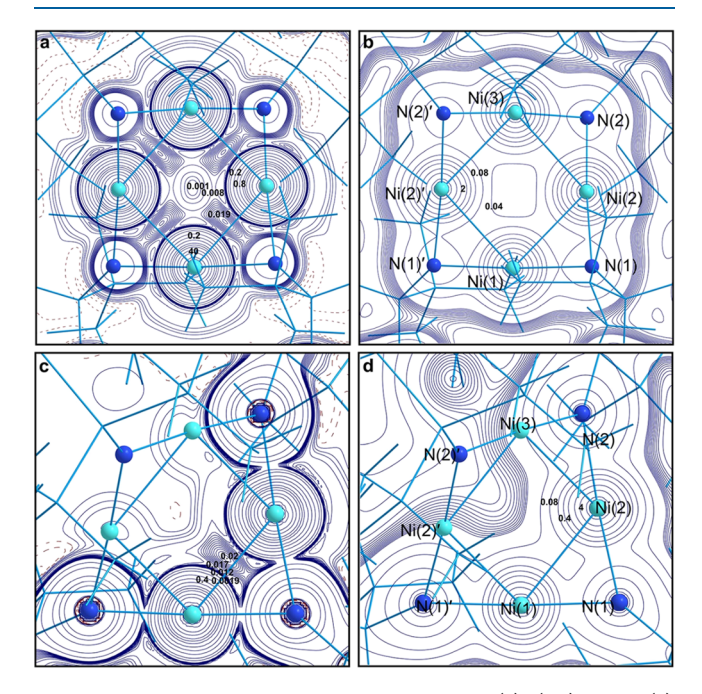


Figure 5. Two-dimensional contour maps of  $K(\mathbf{r})$  (a,c) and  $\rho(\mathbf{r})$  (b,d) for the theoretical wavefunction of 1 plotted in the Ni<sub>4</sub>-plane (upper) and in the Ni(1)–Ni(1)–Ni(2) plane (lower). Selected contour values are shown in Hartree/ų and e/ų for  $K(\mathbf{r})$  and  $\rho(\mathbf{r})$ , respectively. Contour values used for plotting are listed in the Supporting Information.

interatomic interaction energies and explore a global measure of chemical bonding. The interaction energy,  $E_{\rm int}^{\rm AB}$ , is the sum of a Coulombic contribution,  $V_{\rm cl}^{\rm AB}$ , and an exchange correlation contribution,  $V_{\rm xc}^{\rm AB}$ , that can be interpreted as a covalent term (see the Experimental Section and eq 9 for details). The IQA energies for 1 are listed in Table 1. The interaction energy between neighboring Ni centers is negative and thus constitutes a stabilizing interaction. The Coulombic contribu-

Table 1. Table of IQA Energetic Profiles for the Theoretical Model of  $\mathbf{1}^a$ 

| atom pair    | $E_{ m int}^{ m AB}$ | $V_{ m cl}^{ m AB}$ | $V_{ m xc}^{ m AB}$ |
|--------------|----------------------|---------------------|---------------------|
| Ni(1)-Ni(2)  | -0.0152              | 0.0797              | -0.0948             |
| Ni(2)-Ni(3)  | -0.0162              | 0.0789              | -0.0951             |
| Ni(1)-Ni(3)  | 0.0310               | 0.0387              | -0.0076             |
| Ni(2)-Ni(2)' | 0.0329               | 0.0463              | -0.0133             |
| Ni-N(avg.)   | -0.4756              | -0.3027             | -0.1729             |

<sup>a</sup>The term  $E_{\text{int}}^{\text{AB}}$  is the interaction energy between atoms A and B,  $V_{\text{cl}}^{\text{AB}}$  is the classical Coulombic interaction energy, and  $V_{\text{cl}}^{\text{xB}}$  is the exchange correlation interaction energy. All energies are listed in atomic units.

tion is necessarily positive, given that the Ni centers are positively charged ions. The negative total IQA energy is therefore a consequence of a strong covalent term, that is, a signature of significant electron sharing between the two atomic basins. In contrast, both pairs of Ni ions related diagonally on the Ni<sub>4</sub>-square exhibit positive overall IQA energies, which can therefore be regarded as destabilizing.

**Bond Delocalization Index.** Highly related to the energetics of the system obtained using the IQA approach are the delocalization indices (Table 2). In well-defined

Table 2. Calculated Delocalization Indices for Selected Atom Pairs in the Central Part of 1 Based on the Theoretical Wavefunction from the DFT Calculation

| atom pair       | delocalization Index |  |
|-----------------|----------------------|--|
| Ni(1)-N(1)      | 0.723                |  |
| $N_i(2) - N(1)$ | 0.729                |  |
| Ni(2)-N(2)      | 0.725                |  |
| Ni(3)-N(2)      | 0.723                |  |
| Ni(1)-Ni(2)     | 0.594                |  |
| Ni(2)-Ni(3)     | 0.596                |  |
| N(1)-P(1)       | 0.842                |  |
| N(2)-P(2)       | 0.843                |  |
| Ni(1)-Ni(3)     | 0.071                |  |
| Ni(2)-Ni(2)'    | 0.107                |  |

molecular systems of lighter elements, the delocalization index represents the number of electron pairs shared between two atoms, irrespective of whether the two atoms involved share a bond critical point. The situation is a little less clear when metal atoms are involved and bond orders of significantly less than unity are found, even when bond critical points are present. For instance, in the unbridged  $D_{\rm 3d}$  isomer of  ${\rm Co_2(CO)_8}$ , which has a bond critical point at the Co–Co midpoint, the Co–Co delocalization index is 0.48. For the corresponding bridged  $C_{\rm 2v}$  isomer with no Co–Co bond critical point; however, the delocalization index is slightly smaller at 0.37.

Although no Ni–Ni bond critical points were found in the analysis of the experimental electron density of 1, the delocalization indices between pairs of neighboring Ni atoms were found to be ~0.6 (Table 2). The size of these delocalization indices suggests relatively strong interactions between the neighboring Ni atoms in 1 and is only slightly smaller than the ones found for the ligand Ni-N interactions being ~0.7. The ligand—metal delocalization indices fit well with other reported metal—ligand delocalization indices. For example, in dimeric copper and silver *m*-terphenyl complexes with comparable metal coordination geometries and short

metal–metal distances, the delocalization indices between each metal and the bridging carbon atom of the m-terphenyl ligand were found to be in the range 0.51-0.61. For the bridged  $C_{2v}$  isomer of  $Co_2(CO)_8$ , the delocalization indices between the cobalt centers and the bridging CO were found to have an average value of around 0.82.

Comparison of the magnitude of the Ni–N and Ni–Ni delocalization indices offers a simplistic, yet intuitive interpretation of the delocalization indices: At each corner of the Ni<sub>4</sub>N<sub>4</sub>-square, there is a Ni<sub>2</sub>N triangle (e.g., Ni(1)–N(1)–Ni(2)). Within each interaction triangle, two electron pairs are shared, and each of three interactions in the triangle has a bond order of around 2/3.

The strong Ni–Ni interactions are predominantly present between the neighboring Ni atoms, as much lower values are found for the delocalization indices between Ni atoms across the diagonal of the  $Ni_4$ -square (0.071 and 0.107 for Ni(1)–Ni(3) and Ni(2)–Ni(2)′, respectively).

A total delocalization index of 2.6 is obtained for all six individual Ni–Ni interactions, including the two Ni–Ni interactions across the diagonal (Table 2). This may be compared to the bond orders obtained from the previously published DFT calculations on this complex.<sup>8</sup> One interpretation of the molecular orbitals in that study of 1 is that a total of 4 electrons take part in direct Ni–Ni bonding, or a total bond order of 2.0, comparable to the value of 2.6 found here

#### CONCLUSIONS

We have developed experimental and theoretical models of the electron density in  $Ni_4(NP^tBu_3)_4$  (1) based on high-resolution single-crystal synchrotron X-ray diffraction data, in an attempt to better understand the proposed metal–metal bonding interactions in this structure. Despite the exceptional quality of the diffraction data and derived multipole models for  $Ni_4(NP^tBu_3)_4$ , the topological analysis of the electron density of the metal–metal bonding in the molecule proved to be challenging.

The analysis of the static deformation density and the Laplacian distribution did not reveal any clear indication of intramolecular Ni–Ni bonding, due to the overwhelming contribution from the stronger Ni–N interactions. Furthermore, topological analysis of the electron density showed no bond critical points between Ni centers; however, some additional critical points were present in the analysis of the energy density. The interacting quantum atom approach revealed that interactions between neighboring Ni atoms—but not those across the diagonal—do indeed stabilize the complex via a dominant covalent interaction energy. In addition, the delocalization indices gave strong indications of delocalized electron density between the neighboring Ni atoms, giving almost similar-sized values for metal—metal and metal—ligand pairs.

The results from the topological analysis of the experimental electron density highlight the challenges encountered in the characterization of metal—metal bonding interactions. The relatively flat electron density landscape in the interatomic regions is often overwhelmed by the stronger nearby metal—ligand interactions, rendering the study of metal—metal interactions difficult. In the context of the magnetic interactions, the current analysis shows that Ni—Ni interactions are in fact present. The bonding interaction allows the kinetic energy of the electrons to overcome the pairing energy

of a bond, which is critical for ensuring maximal spin in accordance with Hund's rule via electron exchange pathways. Therefore, we reason that the metal—metal interactions of the type evaluated here are key to the intriguing magnetic properties of such molecules.

#### ASSOCIATED CONTENT

#### Supporting Information

The Supporting Information is available free of charge at https://pubs.acs.org/doi/10.1021/acs.inorgchem.2c03170.

Information about data and model quality; DRK plots; fractal dimensionality plots; structural results; theoretical molecular orbitals; topological analysis; and d-orbital populations (PDF)

#### **Accession Codes**

CCDC 2209122 contains the supplementary crystallographic data for this paper. These data can be obtained free of charge via <a href="https://www.ccdc.cam.ac.uk/data\_request/cif">www.ccdc.cam.ac.uk/data\_request/cif</a>, or by emailing data\_request@ccdc.cam.ac.uk, or by contacting The Cambridge Crystallographic Data Centre, 12 Union Road, Cambridge CB2 1EZ, UK; fax: +44 1223 336033.

#### AUTHOR INFORMATION

#### **Corresponding Author**

Jacob Overgaard — Department of Chemistry, Aarhus University, DK-8000 Aarhus C, Denmark; ⊚ orcid.org/0000-0001-6492-7962; Email: jacobo@chem.au.dk

#### **Authors**

Sofie Stampe Leiszner – Department of Chemistry, Aarhus University, DK-8000 Aarhus C, Denmark; ⊙ orcid.org/ 0000-0003-0614-8009

Khetpakorn Chakarawet – Department of Chemistry, University of California, Berkeley, Berkeley, California 94720, United States

Jeffrey R. Long — Department of Chemistry and Department of Chemical and Biomolecular Engineering, University of California, Berkeley, Berkeley, California 94720, United States; Materials Sciences Division, Lawrence Berkeley National Laboratory, Berkeley, California 94720, United States; orcid.org/0000-0002-5324-1321

Eiji Nishibori — Department of Physics, Faculty of Pure and Applied Sciences, Tsukuba Research Center for Energy Materials Science (TREMS), University of Tsukuba, Tsukuba 3058571, Japan; orcid.org/0000-0002-4192-6577

Kunihisa Sugimoto — Diffraction & Scattering Division Synchrotron Radiation Research Institute, Hyogo 679-5198, Japan; © orcid.org/0000-0002-0103-8153

James A. Platts — School of Chemistry, Cardiff University, Cardiff CF10 3AT, U.K.; orcid.org/0000-0002-1008-6595

Complete contact information is available at: https://pubs.acs.org/10.1021/acs.inorgchem.2c03170

#### **Author Contributions**

The manuscript was written through contributions of all authors. All authors have given approval to the final version of the manuscript.

#### **Funding**

Danscatt. Villum Foundation. Novo Nordisk Foundation.

#### Notes

The authors declare no competing financial interest.

#### ACKNOWLEDGMENTS

Affiliation with the Center for Integrated Materials Research (iMAT) at Aarhus University and funding from the Danish Ministry of Higher Education and Science through the SMART Lighthouse is gratefully acknowledged. J.O. and S.S.L. acknowledge financial support from Aarhus University Research Foundation, the Villum Foundation, Novo Nordisk Foundation, and Danscatt. J.R.L. and K.C. acknowledge NSF grant CHE-2102603 for the synthesis of the materials. The synchrotron experiment was performed on beamline BL02B1 at SPring-8 with the approval of the Japan Synchrotron Radiation Research Institute as a Partner User (proposal No. 2018B0078).

#### REFERENCES

- (1) Damgaard-Moller, E.; Krause, L.; Lassen, H.; Malaspina, L. A.; Grabowsky, S.; Bamberger, H.; McGuire, J.; Miras, H. N.; Sproules, S.; Overgaard, J. Investigating Complex Magnetic Anisotropy in a Co(II) Molecular Compound: A Charge Density and Correlated Ab Initio Electronic Structure Study. *Inorg. Chem.* **2020**, *59*, 13190–13200.
- (2) Gould, C. A.; McClain, K. R.; Reta, D.; Kragskow, J. G. C.; Marchiori, D. A.; Lachman, E.; Choi, E. S.; Analytis, J. G.; Britt, R. D.; Chilton, N. F.; Harvey, B. G.; Long, J. R. Ultrahard magnetism from mixed-valence dilanthanide complexes with metal-metal bonding. *Science* 2022, 375, 198–202.
- (3) Sanchez, R. H.; Betley, T. A. Thermally Persistent High-Spin Ground States in Octahedral Iron Clusters. *J. Am. Chem. Soc.* **2018**, 140, 16792–16806.
- (4) Sanchez, R. H.; Bartholomew, A. K.; Powers, T. M.; Menard, G.; Betley, T. A. Maximizing Electron Exchange in a [Fe3] Cluster. *J. Am. Chem. Soc.* **2016**, *138*, 2235–2243.
- (5) Sanchez, R. H.; Zheng, S. L.; Betley, T. A. Ligand Field Strength Mediates Electron Delocalization in Octahedral [((H)L)2Fe6(L')-m](n+) Clusters. *J. Am. Chem. Soc.* **2015**, *137*, 11126–11143.
- (6) Cook, A. W.; Bocarsly, J. D.; Lewis, R. A.; Touchton, A. J.; Morochnik, S.; Hayton, T. W. An iron ketimide single-molecule magnet [Fe4(N=CPh2)6] with suppressed through-barrier relaxation. *Chem. Sci.* **2020**, *11*, 4753–4757.
- (7) Camacho-Bunquin, J.; Ferguson, M. J.; Stryker, J. M. Hydrocarbon-soluble nanocatalysts with no bulk phase: coplanar, two-coordinate arrays of the base metals. *J. Am. Chem. Soc.* **2013**, *135*, 5537–5540.
- (8) Chakarawet, K.; Atanasov, M.; Marbey, J.; Bunting, P. C.; Neese, F.; Hill, S.; Long, J. R. Strong Electronic and Magnetic Coupling in M4 (M = Ni, Cu) Clusters via Direct Orbital Interactions between Low-Coordinate Metal Centers. *J. Am. Chem. Soc.* **2020**, *142*, 19161–19169.
- (9) Chakarawet, K.; Bunting, P. C.; Long, J. R. Large Anisotropy Barrier in a Tetranuclear Single-Molecule Magnet Featuring Low-Coordinate Cobalt Centers. J. Am. Chem. Soc. 2018, 140, 2058–2061.
- (10) Bader, R. F. W. Atoms in Molecules: A Quantum Theory; Clarendon Press: Oxford, 1990; p xviii, p 438.
- (11) Gervasio, G.; Bianchi, R.; Marabello, D. Unexpected intramolecular interactions in Ru-3(CO)(12): An experimental charge density study at 120 K. Chem. Phys. Lett. 2005, 407, 18–22.
- (12) Gervasio, G.; Bianchi, R.; Marabello, D. About the topological classification of the metal-metal bond. *Chem. Phys. Lett.* **2004**, 387, 481–484.
- (13) Bianchi, R.; Gervasio, G.; Marabello, D. An experimental evidence of a metal-metal bond in mu-carbonylhexacarbonyl mu-(5-oxofuran-2(5H)-ylidene-kappa C,kappa C) dicobalt(Co-Co) Co-2(CO)(6)(mu-CO)(mu-C4O2H2). *Helv. Chim. Acta* **2001**, *84*, 722–734.

- (14) Bianchi, R.; Gervasio, G.; Marabello, D. Experimental electron density in the triclinic phase of Co-2(CO)(6)(mu-CO)(mu-C4O2H2) at 120 K. Acta Crystallogr., Sect. B: Struct. Sci., Cryst. Eng. Mater. 2001, 57, 638–645.
- (15) Bianchi, R.; Gervasio, G.; Marabello, D. Experimental Electron Density Analysis of Mn2(CO)10: Metal–Metal and Metal–Ligand Bond Characterization. *Inorg. Chem.* **2000**, *39*, 2360–2366.
- (16) Bianchi, R.; Gervasio, G.; Marabello, D. Experimental charge density study of the Mn-Mn bond in Mn2(CO)10 at 120 K. *Chem. Commun.* 1998, 1535–1536.
- (17) Farrugia, L. J.; Macchi, P. Bond Orders in Metal-Metal Interactions Through Electron Density Analysis. In *Electron Density and Chemical Bonding I: Experimental Charge Density Studies*, 2012; Vol. 146, pp 127 –158.
- (18) Farrugia, L. J.; Evans, C.; Senn, H. M.; Hanninen, M. M.; Sillanpaa, R. QTAIM View of Metal-Metal Bonding in Di- and Trinuclear Disulfido Carbonyl Clusters. *Organometallics* **2012**, *31*, 2559–2570.
- (19) Farrugia, L. J. Is there a Co-Co bond path in Co-2(CO) (6)(mu-CO)(mu-C4H2O2)? Chem. Phys. Lett. **2005**, 414, 122–126.
- (20) Farrugia, L. J.; Evans, C. Metal-metal bonding in bridged ligand systems: experimental and theoretical charge densities in  $Co3(\mu3-CX)(CO)9$  (X = H, Cl). C. R. Chim. 2005, 8, 1566–1583.
- (21) Farrugia, L. J.; Mallinson, P. R.; Stewart, B. Experimental charge density in the transition metal complex Mn2(CO)10: a comparative study. *Acta Crystallogr., Sect. B: Struct. Sci.* **2003**, *59*, 234–247.
- (22) Overgaard, J.; Jones, C.; Stasch, A.; Iversen, B. B. Experimental Electron Density Study of the Mg-Mg Bonding Character in a Magnesium(I) Dimer. *J. Am. Chem. Soc.* **2009**, *131*, 4208–4209.
- (23) Overgaard, J.; Platts, J. A.; Iversen, B. B. Experimental and theoretical charge-density study of a tetranuclear cobalt carbonyl complex. *Acta Crystallogr., Sect. B: Struct. Sci., Cryst. Eng. Mater.* **2009**, 65, 715–723.
- (24) Poulsen, R. D.; Overgaard, J.; Schulman, A.; Ostergaard, C.; Murillo, C. A.; Spackman, M. A.; Iversen, B. B. Effects of Weak Intermolecular Interactions on the Molecular Isomerism of Tricobalt Metal Chains. *J. Am. Chem. Soc.* **2009**, *131*, 7580–7591.
- (25) Clausen, H. F.; Overgaard, J.; Chen, Y. S.; Iversen, B. B. Synchrotron X-ray charge density study of coordination polymer Co3(C8H4O4)4(C4H12N)2(C5H11NO)3 at 16 K. J. Am. Chem. Soc. 2008, 130, 7988–7996.
- (26) Overgaard, J.; Clausen, H. F.; Platts, J. A.; Iversen, B. B. Experimental and theoretical charge density study of chemical bonding in a Co dimer complex. *J. Am. Chem. Soc.* **2008**, *130*, 3834–3843.
- (27) Platts, J. A.; Evans, G. J.; Coogan, M. P.; Overgaard, J. Electronic structure of the alkyne-bridged dicobalt hexacarbonyl complex Co(2) micro-C(2)H(2) (CO)(6): evidence for singlet diradical character and implications for metal-metal bonding. *Inorg. Chem.* **2007**, *46*, 6291–6298.
- (28) Macchi, P.; Garlaschelli, L.; Martinengo, S.; Sironi, A. Charge Density in Transition Metal Clusters: Supported vs Unsupported Metal—Metal Interactions. *J. Am. Chem. Soc.* **1999**, *121*, 10428—10429.
- (29) Krause, L. pilatus3-fc, 2019.
- (30) APEX3. v2018.7-2; 2018.
- (31) Bruker, A. APEX3, SAINT-Plus and SADABS. Bruker AXS Inc., Madison, Wisconsin, USA, 2016.
- (32) Krause, L.; Herbst-Irmer, R.; Sheldrick, G. M.; Stalke, D. Comparison of silver and molybdenum microfocus X-ray sources for single-crystal structure determination. *J. Appl. Crystallogr.* **2015**, 48, 3–10.
- (33) Blessing, R. H. DREAM data reduction and error analysis routines for accurate single-crystal diffraction intensity measurements. *J. Appl. Crystallogr.* **1986**, *19*, 412.
- (34) Sheldrick, G. SHELXT Integrated space-group and crystal-structure determination. *Acta Crystallogr., Sect. A: Found. Adv.* **2015**, 71, 3–8.

- (35) Sheldrick, G. M. A short history of SHELX. Acta Crystallogr., Sect. A: Found. Adv. 2008, 64, 112–122.
- (36) Volkov, A.; Macchi, P.; Farrugia, L. J.; Gatti, C.; Mallinson, P.; Richter, T.; Koritsanszky, T. XD2006 A Computer Program Package for Multipole Refinement, Topological Analysis of Charge Densities and Evaluation of Intermolecular Energies from Experimental and Theoretical Structure Factors, 2006.
- (37) Hansen, N. K.; Coppens, P. Electron Population Analysis of Accurate Diffraction Data .6. Testing Aspherical Atom Refinements on Small-Molecule Data Sets. *Acta Crystallogr., Sect. A: Found. Adv.* 1978, 34, 909–921.
- (38) Damgaard-Møller, E.; Krause, L.; Overgaard, J., Experimental Charge Densities from Multipole Modeling: Moving into the Twenty-First Century. In 21st Century Challenges in Chemical Crystallography II, Mingos, D. M. P.; Raithby, P. R., Eds.; Springer International Publishing: Cham, 2020; pp 145–182.
- (39) Coppens, P. X-Ray Charge Densities and Chemical Bonding (IUCr Texts on Crystallography); IUCr, 1997; p 384.
- (40) Allen, F. H.; Kennard, O.; Watson, D. G.; Brammer, L.; Orpen, A. G.; Taylor, R. Tables of bond lengths determined by X-ray and neutron diffraction. Part 1. Bond lengths in organic compounds. *J. Chem. Soc., Perkin Trans.* 2 **1987**, S1–S19.
- (41) Niepotter, B.; Herbst-Irmer, R.; Stalke, D. Empirical correction for resolution- and temperature-dependent errors caused by factors such as thermal diffuse scattering. *J. Appl. Crystallogr.* **2015**, *48*, 1485–1497.
- (42) Meindl, K.; Henn, J. Foundations of residual-density analysis. *Acta Crystallogr., Sect. A: Found. Adv.* **2008**, *64*, 404–418.
- (43) Genoni, A. On the use of the Obara-Saika recurrence relations for the calculation of structure factors in quantum crystallography. *Acta Crystallogr., Sect. A: Found. Adv.* **2020**, *76*, 172–179.
- (44) Neese, F. The ORCA program system. Wiley Interdiscip. Rev.: Comput. Mol. Sci. 2012, 2, 73–78.
- (45) Neese, F. Software update: the ORCA program system, version 4.0. Wiley Interdiscip. Rev.: Comput. Mol. Sci. 2018, 8, No. e1327.
- (46) Cremer, D.; Kraka, E. Chemical-Bonds without Bonding Electron-Density Does the Difference Electron-Density Analysis Suffice for a Description of the Chemical-Bond. *Angew. Chem., Int. Ed.* **1984**, 23, 627–628.
- (47) Cremer, D.; Kraka, E. A Description of the Chemical-Bond in Terms of Local Properties of Electron-Density and Energy. *Croat. Chem. Acta* 1984, 57, 1259–1281.
- (48) Keith, T. A. AIMAll, 19.10.12; TK Gristmill Software: Overland Park KS, USA, 2019.
- (49) Tiana, D.; Francisco, E.; Blanco, M. A.; Macchi, P.; Sironi, A.; Martin Pendas, A. Bonding in Classical and Nonclassical Transition Metal Carbonyls: The Interacting Quantum Atoms Perspective. *J. Chem. Theory Comput.* **2010**, *6*, 1064–1074.
- (50) Angyan, J. G.; Loos, M.; Mayer, I. Covalent Bond Orders and Atomic Valence Indexes in the Topological Theory of Atoms in Molecules. *J. Phys. Chem.* **1994**, *98*, 5244–5248.
- (51) Fradera, X.; Austen, M. A.; Bader, R. F. W. The Lewis model and beyond. J. Phys. Chem. A 1999, 103, 304-314.
- (52) Farrugia, L. J.; Senn, H. M. Metal-metal and metal-ligand bonding at a QTAIM catastrophe: a combined experimental and theoretical charge density study on the alkylidyne cluster Fe3(mu-H)(mu-COMe)(CO)10. J. Phys. Chem. A 2010, 114, 13418–13433.
- (53) Cotton, F. A.; Murillo, C. A.; Walton, R. A. Multiple Bonds Between Metal Atoms. 3rd ed.; Springer-Verlag New York, 2005.
- (54) Stalke, D. Meaningful Structural Descriptors from Charge Density. Chem. Eur. J. 2011, 17, 9264–9278.
- (55) Mebs, S.; Henn, J.; Dittrich, B.; Paulmann, C.; Luger, P. Electron densities of three B12 vitamins. *J. Phys. Chem. A* **2009**, *113*, 8366–8378.
- (56) Finger, M.; Reinhold, J. Energy density distribution in bridged cobalt complexes. *Inorg. Chem.* **2003**, 42, 8128–8130.
- (57) Reinhold, J.; Kluge, O.; Mealli, C. Integration of electron density and molecular orbital techniques to reveal questionable

bonds: the test case of the direct Fe-Fe bond in Fe2(CO)9. *Inorg. Chem.* **2007**, *46*, 7142–7147.

- (58) Macchi, P.; Garlaschelli, L.; Sironi, A. Electron density of semi-bridging carbonyls. Metamorphosis of CO Ligands observed via experimental and theoretical investigations on FeCo(CO)(8) (–). *J. Am. Chem. Soc.* **2002**, *124*, 14173–14184.
- (59) Bauschlicher, C. W. On the bonding in Fe2(CO)9. *J. Chem. Phys.* **1986**, 84, 872–875.
- (60) Bo, C.; Sarasa, J. P.; Poblet, J. M. Laplacian of Charge-Density for Binuclear Complexes Terminal Vs Bridging Carbonyls. *J. Phys. Chem.* **1993**, 97, 6362–6366.
- (61) Tiana, D.; Francisco, E.; Macchi, P.; Sironi, A.; Martín Pendás, A. An Interacting Quantum Atoms Analysis of the Metal–Metal Bond in [M2(CO)8]n Systems. *J. Phys. Chem. A* **2015**, *119*, 2153–2160.
- (62) Macchi, P.; Sironi, A. Chemical bonding in transition metal carbonyl clusters: complementary analysis of theoretical and experimental electron densities. *Coord. Chem. Rev.* **2003**, 238, 383–412.
- (63) Liu, Y.; Taylor, L. J.; Argent, S. P.; McMaster, J.; Kays, D. L. Group 11 m-Terphenyl Complexes Featuring Metallophilic Interactions. *Inorg. Chem.* **2021**, *60*, 10114–10123.

### ☐ Recommended by ACS

## Influence of Pd(II) Adsorption on High-Temperature Ferroelastic Phase Transition in (2-Amino-2-thiazolinium)PbBr<sub>3</sub>

Yan Xu, Qiong Ye, et al.

JANUARY 07, 2023
INORGANIC CHEMISTRY

READ 🗹

## Two-Electron Mixed Valency in a Heterotrimetallic Nickel-Vanadium-Nickel Complex

Michael K. Wojnar, Alan F. Heyduk, et al.

JANUARY 12, 2023 INORGANIC CHEMISTRY

READ 🗹

### One Bridge, Three Bonds: A Frontier in Multiple Bonding in Heterobimetallic Complexes

Nathanael H. Hunter, Christine M. Thomas, et al.

JANUARY 03, 2023 INORGANIC CHEMISTRY

READ [7

## Development of Porous Crystalline Materials for Selective Binding of O<sub>2</sub> from Air

Jifeng Sun, David S. Sholl, et al.

DECEMBER 30, 2022

THE JOURNAL OF PHYSICAL CHEMISTRY C

READ 🗹

Get More Suggestions >